Appl. Math. Mech. -Engl. Ed., 2008, **29**(3):351–360
DOI 10.1007/s10483-008-0306-y

Applied Mathematics and Mechanics (English Edition)

Numerical investigations on dynamic process of muzzle flow *

JIANG Xiao-hai (姜孝海), FAN Bao-chun (范宝春), LI Hong-zhi (李鸿志)

(National Key Laboratroy of Transient Physics, Nanjing University of Science and Technology, Nanjing 210094, P. R. China)

(Communicated by SONG Shun-cheng)

Abstract The integrative process of a quiescent projectile accelerated by high-pressure gas to shoot out at a supersonic speed and beyond the range of a precursor flow field was simulated numerically. The calculation was based on ALE equations and a second-order precision Roe method that adopted chimera grids and a dynamic mesh. From the predicted results, the coupling and interaction among the precursor flow field, propellant gas flow field and high-speed projectile were discussed in detail. The shock-vortex interaction, shockwave reflection, shock-projectile interaction with shock diffraction, and shock focus were clearly demonstrated to explain the effect on the acceleration of the projectile.

Key words gasdynamics, numerical simulation, muzzle flow, dynamic process

Chinese Library Classification TJ012.2
2000 Mathematics Subject Classification 76J20, 76L05

Introduction

A blast wave, strong radiation, noise and other events occur in the vicinity of the muzzle when a projectile accelerated by high-temperature high-pressure propellant gas shoots out. These could cause some damage to the gun crew, surroundings and firing accuracy. Therefore, it is of practical importance to investigate the muzzle flow for weapon improvement and design. Research about this high transient supersonic flow, coupled with strong discontinuity, chemical reaction and high-speed moving projectile, is still in development[1−6]. It is a viable alternative to adopt the CFD (computational fluid dynamics) method[3,4,6], considering the experiment's cost and potential danger, device limitation and uncertainty.

The FREIN code based on two-dimensional Euler equations and the TVD scheme was adopted by Cayzac et al. to predict the flow with the muzzle precursor flowfield, moving projectile and muzzle brakes[7]. Later the APFSDS sabot separation process[8] was also simulated. The boundary at the barrel muzzle was computed using an 1D numerical code based on the characteristics method according to pull piston analogy. Jiang[3, 9] used a second-order dispersion-controlled scheme based on axisymmetric Euler equations and moving boundary to predict the muzzle flow at different projectile speeds and friction forces. Its initial condition and friction force were implemented through some special assumptions, particularly with the projectile speed and distance between projectile front and exit in the initial stage given. It

* Received Aug. 23, 2007 / Revised Jan. 17, 2008
Project supported by the National Key Laboratory of Transient Physics of China
Corresponding author JIANG Xiao-hai, Doctor, E-mail: xhjiang@mail.njust. edu.cn

is assumed that the precursor shock wave just reached the exit and the initial flow state behind the shock wave was calculated with the standard adiabatic shock relations. Friction force change was obtained by changing the ratio of the pressure of the projectile front to the back. Software package Fluent 6.1 (an second-order inviscid solver) and DGM (based on the Galerkin method) were used by Cler[4] to predict the muzzle flow excluding the moving projectile. Its comparison with the experimental shadowgraph (7.62 mm NATO rifle G3) showed that the precursor results matched the experimental well, but the main propellant flow did not match. Dayan and Touati Cler[6] divided the muzzle flow calculation into two stages. The first covered pressure and temperature, with the projectile motion obtained via the internal ballistics calculation software package IBHVG2, while the second covered the projectile movement in the outer flow simulated via a CFD-FASTRAN finite volume solver package. In general, very good agreements were acquired between the predicted results and the experimentals in the first or second stage, respectively.

In the present paper, the integrative process of a quiescent projectile driven by high-pressure gas to shoot out at a supersonic speed and fly beyond the effective range of a precursor flow field was simulated by using a dynamic mesh and moving boundary based on ALE equations and a second-order Roe method. From the predicted results, the dynamic process of the muzzle flow was discussed in detail.

1 Governing equations

Assuming that the effect of viscosity and chemical reaction is negligible, the ALE (Arbitrary Lagrangian-Eulerian) equation[10] in a time-dependent control volume can be expressed as

$$\frac{\partial}{\partial t}\iiint_{V(t)} \boldsymbol{Q}dV + \oiint_{S(t)} (F - QV_b)\cdot nds = 0, \tag{1}$$

where $\boldsymbol{Q} = [\rho, \rho\boldsymbol{U}, E]^{\mathrm{T}}$, $\boldsymbol{F} = \boldsymbol{Q}\boldsymbol{U} + \boldsymbol{G}$, and $\boldsymbol{G} = [0, p\boldsymbol{n}, p\boldsymbol{U}\cdot\boldsymbol{n}]^{\mathrm{T}}$. ρ, p is the density and pressure respectively, $\boldsymbol{U}$ is the fluid velocity, and E is total energy per unit volume. $S(t)$ is the surface which encloses the time dependent volume $V(t)$. $\boldsymbol{n}$ is the outward unit vector normal to the boundary $S(t)$. $\boldsymbol{V}_b$ is the surface velocity of the time dependent volume.

Define $\boldsymbol{F}$ as $\boldsymbol{F} = \boldsymbol{Q}(\boldsymbol{U} - \boldsymbol{V}_b) + \boldsymbol{G}$, equation (1) can be expressed as

$$\frac{\partial}{\partial t}\iiint_{V(t)} \boldsymbol{Q}dV + \oiint_{S(t)} F\cdot nds = 0. \tag{2}$$

Equation (2) represents the conservation of mass, momentum and energy. Let γ be the ratio of specific heats, then for a perfect gas

$$p = (\gamma - 1)\rho e, \tag{3}$$

where $e = \frac{E}{\rho} - \frac{1}{2}\boldsymbol{U}\cdot\boldsymbol{U}$, it is the specific internal energy.

Equation (2) was discretized on the time-dependent control volume, and after algebraic manipulation, the discretization equation can be written as

$$\boldsymbol{Q}^{n+1} = \frac{V^n}{V^{n+1}}\left(\boldsymbol{Q}^n - \frac{1}{V^n}\sum_{i=1}^{N}\boldsymbol{F}_i\Delta S_i\Delta t\right), \tag{4}$$

where the superscript n denotes the previous time and $n+1$ is the solution time. N is the total number of the surfaces covering the control volume. ΔS_i denotes the i'th surface area, and $\boldsymbol{F}_i$ is its flux.

Considering the control volume interface as a one-dimensional Riemann solution, the interface flux is calculated by using a Roe method, i.e., namely, its flux is related to the cell-centered values of both of its sides and expressed as(for a non-moving grid)

$$\boldsymbol{F}_i^{\mathrm{F}} = \boldsymbol{F}_i^{\mathrm{F}}(\boldsymbol{Q}_{\mathrm{R}}, \boldsymbol{Q}_{\mathrm{L}}) \rightarrow \boldsymbol{A}^{\mathrm{F}} = \frac{\partial \boldsymbol{F}^{\mathrm{F}}}{\partial Q}, \tag{5}$$

$$\boldsymbol{F}_i^{\mathrm{F}} = \frac{1}{2}[\boldsymbol{F}^{\mathrm{F}}(\boldsymbol{Q}_{\mathrm{R}}) + \boldsymbol{F}^{\mathrm{F}}(\boldsymbol{Q}_{\mathrm{L}}) - \sum \boldsymbol{\alpha}_j |\boldsymbol{\Lambda}^{\mathrm{F}}| \boldsymbol{e}_j], \tag{6}$$

where $\boldsymbol{Q}_L$,$\boldsymbol{Q}_R$ denote the cell-centered values of the left and right side of the interface, respectively. $\boldsymbol{\alpha}$, $\boldsymbol{\Lambda}$, $\boldsymbol{e}$ are the wave strength, characteristic matrix and right eigenvectors matrix of the Roe-averaged Jacobian $\boldsymbol{A}^{\mathrm{F}}$, respectively. From mathematical analysis, the grid motion only affects the eigenvalues of the Jacobian matrix, i.e., $\boldsymbol{\Lambda}^{\mathrm{M}} = \boldsymbol{\Lambda}^{\mathrm{F}} - \boldsymbol{V}_b \cdot \boldsymbol{n}$, and wave strength and the left and right eigenvectors are the same as those of the static grid. Thus,

$$\boldsymbol{F}_i^{\mathrm{M}} = \frac{1}{2}[\boldsymbol{F}^{\mathrm{M}}(\boldsymbol{Q}_{\mathrm{R}}) + \boldsymbol{F}^{\mathrm{M}}(\boldsymbol{Q}_{\mathrm{L}}) - \sum \boldsymbol{\alpha}_j |\boldsymbol{\Lambda}_j^{\mathrm{M}}| \boldsymbol{e}_j]. \tag{7}$$

The superscript F and M above denote the static and moving grid, respectively.

To obtain a high-resolution solution, a second-order correction[11] is introduced:

$$\tilde{\boldsymbol{F}}_i = \frac{1}{2} \sum |\lambda_i| \left(1 - \frac{\Delta t}{\Delta x} |\lambda_i|\right) \boldsymbol{W}_i, \tag{8}$$

where $\boldsymbol{Q}_i - \boldsymbol{Q}_{i-1} = \sum_p^m \boldsymbol{W}_i^p \equiv \sum_p^m \boldsymbol{\alpha}_i^p \boldsymbol{r}_i^p$. Therefore, the interface flux is denoted as follows:

$$\boldsymbol{F}_i = \frac{1}{2}[\boldsymbol{F}^{\mathrm{M}}(\boldsymbol{Q}_R) + \boldsymbol{F}^{\mathrm{M}}(\boldsymbol{Q}_L) - \sum \boldsymbol{\alpha}_j |\boldsymbol{\Lambda}_j^{\mathrm{M}}| \boldsymbol{e}_j] + \frac{1}{2} \sum |\lambda_i| \left(1 - \frac{\Delta t}{\Delta x} |\lambda_i|\right) \boldsymbol{W}_i. \tag{9}$$

In the transonic or supersonic case, spurious oscillations near discontinuities generally appear. Limiter functions, called flux limiters or wave limiters, are thus applied to suppress these oscillations, i.e.,

$$\boldsymbol{W}_i = \tilde{\boldsymbol{\alpha}}_i \boldsymbol{r}, \tag{10}$$

where $\tilde{\boldsymbol{\alpha}}_i^p = \phi(\theta_i^p) \boldsymbol{\alpha}_i^p$, and

$$\theta_i^p = \frac{\boldsymbol{\alpha}_I^p}{\boldsymbol{\alpha}_i^p}, \quad I = \begin{cases} i-1 & \text{if } \lambda_i^p > 0, \\ i+l & \text{if } \lambda_i^p \leq 0. \end{cases} \tag{11}$$

In the present paper, the value of $\phi(\theta)$ (i.e., the limiter function) is obtained based on the Monotonized centered method[12],

$$\phi(\theta) = \max(0, \min((1+\theta)/2, 2, 2\theta)). \tag{12}$$

Therefore, the second-order accuracy interface flux was obtained and substituted into equation (4) to obtain the next time solution. For time-marching, the second-order Runge-Kutta method was applied.

Due to the grid deformation caused by the projectile motion, the chimera grids method[13] was adopted, namely. It includes the background grid (It is static or stationary) and attached grid (It is movable with the projectile). Shown as Fig. 1(a), the finer grid around the projectile is the attached grid, the coarser grid (including those covered by the projectile and attached grid, which are not taken into the solver in calculation) is the background grid, and the bold line is the interface of their intersection. To reduce interpolation errors of the background and attached grids, their interface are always located on the boundary of the control volumes as

shown in Fig. 1(b), and the velocity in the attached grid was given a certain linear distribution. When the displacement of the projectile exceeds the given criterion, a reconstruction of the attached grid will take place and make it restored to ensure the computation accuracy, as shown in Fig. 1(c). Bilinear interpolation[14] is applied in this reconstruction. Values of the background grids exposed due to this reconstruction of the attached grid at the tail of the projectile would be obtained through the interpolation of the attached grids, while the ones covered by the attached grids in the front of the projectile would be interpolated into the new attached grids.

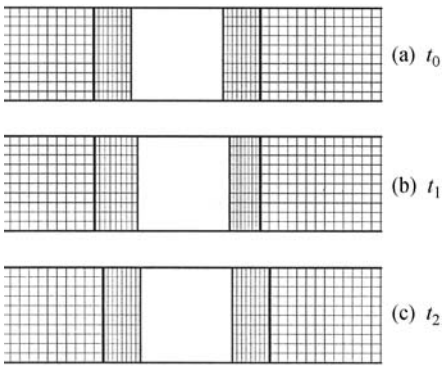

Fig. 1 Schematic diagram of the chimera grids

2 Numerical results and discussion

The present computational domain is schematic in Fig. 2. The length of the gun tube $L_1 = 120$ mm, while its inner and outer calibers are $\Phi_0 = 24$ mm and $\Phi_1 = 44$ mm, respectively. The outer flowfield is also a coaxial cylinder, with diameter and length of $\Phi_2 = 200$ mm and $L_2 = 600$ mm, respectively. During calculation, the gun tube inner caliber Φ_0 is the reference scale. The projectile was also simplified into a cylinder with diameter of Φ_0 (same as the tube inner caliber) and length $\Delta L = \Phi_0 = 24$ mm. In the initial stage, the distance between the projectile and the closed end of the tube is $L_0 = 60$ mm. The tube is separated into two parts by the projectile, i.e., the enclosed powder chamber D_1 and the remaining D_2 connected to the outer ambient air D_3. The computation domain is only the upper half in Fig. 2 considering its axial symmetry, and 1200×200 mesh points were used in the background grid.

There are two boundary conditions used here the solid and out flow boundary. The former includes static solid boundary (i.e., the inner and outer surfaces of the tube) and moving solid boundary (i.e., surfaces of the projectile). Both were assumed as slip boundary, i.e., the normal velocity component of the static solid boundary is zero, while that of the moving solid is equal

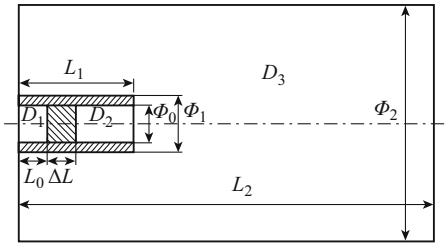

Fig. 2 Schematic of the computational domain

to the component of the moving projectile. Since the latter (out flow boundary) is only affected by the interior, its interface flux is always equal to the flux of the cell-centered values. Because the solid boundary is a slip boundary, the axisymmetric boundary is the same as a static solid boundary.

In the initial stage, it is assumed that the fuel in powder chamber D_1 in Fig. 2 is burned up and its ratio of specific heat is equal to the air in D_2 and D_3. The initial pressure and temperature in D_1 is $p_{\text{in}}^0 = 600.0p_0$ and $T_{\text{in}}^0 = 6.0T_0$, respectively. Here, p_0 and T_0 are the initial (ambient) pressure and temperature in D_2 and D_3, i.e., $T_0 = 298.15$ K, $p_0 = 101325$ Pa. The mass of the projectile is $m = 25$ g, the friction force is proportional to the area of the contact surface between the projectile and the tube, and the friction coefficient is 0.005. The projectile movement acts according to Newton's law and the exit speed is $1.77Ma$ (the ambient sonic speed).

Figure 3 is the predicted isopycnics (the upper half) and isobars (the lower half). Figures 3(a)–(d) show the development of the precursor flow field before the projectile completely shoots out of the tube. The precursor shock wave originated from the gas in D_2, compressed by the moving projectile driven by high-pressure gas in D_1 and becoming increasingly stronger as shown in Fig. 3(a). It later propagates outwards and diffracts at the tube exit to form a sphere-like shape in Fig. 3(b), prior to the projectile reaching the exit. As the high-speed compressed gas (D_2) jets out, the under-expanded jet pattern appears, i.e., the barrel shock wave, shear layer, primary vortex ring and the contact surface, which was the interface of the vented gas (D_2) and the background atmosphere. In Fig. 3(c), the upward-facing shock wave with the shape of a spherical cap is shown, and its rim is sucked into the core of the primary vortex ring to adjust the flow between its wave front zone (i.e., the super-sonic expansion zone towards the tube exit) and the wave back (i.e., behind the precursor shock wave at the back of the tube exit). At the intersection of the projectile head and tube exit, a weak cylindrical shock wave was generated around the projectile due to rising pressure caused by the sudden emergence of the projectile and the effect of the primary vortex ring. In Fig. 3(d), the projectile was about to completely disengage from the exit and the special background precursor flow pattern was formed as shown in this figure.

Figures 3(e)–(g) show the development of propellant flow field and the formation of the bow shock wave in front of the projectile. In Fig. 3(e), the propellant gas rushed out, and the under-expanded flow pattern was similar to previous precursor flow fields, i.e., the shear layer, barrel shock wave, primary vortex ring, and muzzle blast wave. However, its background flow is not the ambient atmosphere, but the aforementioned non-homogeneous precursor flow. The muzzle blast wave propagated mainly in the radial direction with an annulus-like shape due to the effect of the background flow and projectile. In Fig. 3(f), the muzzle blast wave swept through the cylindrical shock to catch up with the projectile. At the same time, the cap-like shock wave (upward-facing shock wave) was split by the projectile and slipped along the side of the projectile. In addition, the detached shock waves started to appear on the edge of the projectile head and then extended towards the axis. In Fig. 3(g), they linked together to form the bow shock wave with a contact surface behind it. This bow shock wave production was related to the projectile moving speed and flow property of the precursor flowfield, i.e., before crossing through the cap-like shock wave, the projectile speed was approximately equal to the particle velocity in the expansion zone, and thus did not appear as the shock wave. However, when it crossed the cap-like shock wave and entered into the subsonic zone (i.e., wave back zone), its speed was practically unaffected due to the inertia. Thus, its speed was supersonic relative to the local particle, resulting in the bow shock wave in front of the projectile.

After the muzzle blast wave reached the affected area of the primary vortex ring, the fold (in the vicinity of the vortex core) and split (close to the projectile side) of its wave front happened as shown in Fig. 3(g). A secondary cap-like shock wave appeared on the side of the projectile between the muzzle blast wave and barrel shock wave (propellant gas flow field). In Fig. 3(h),

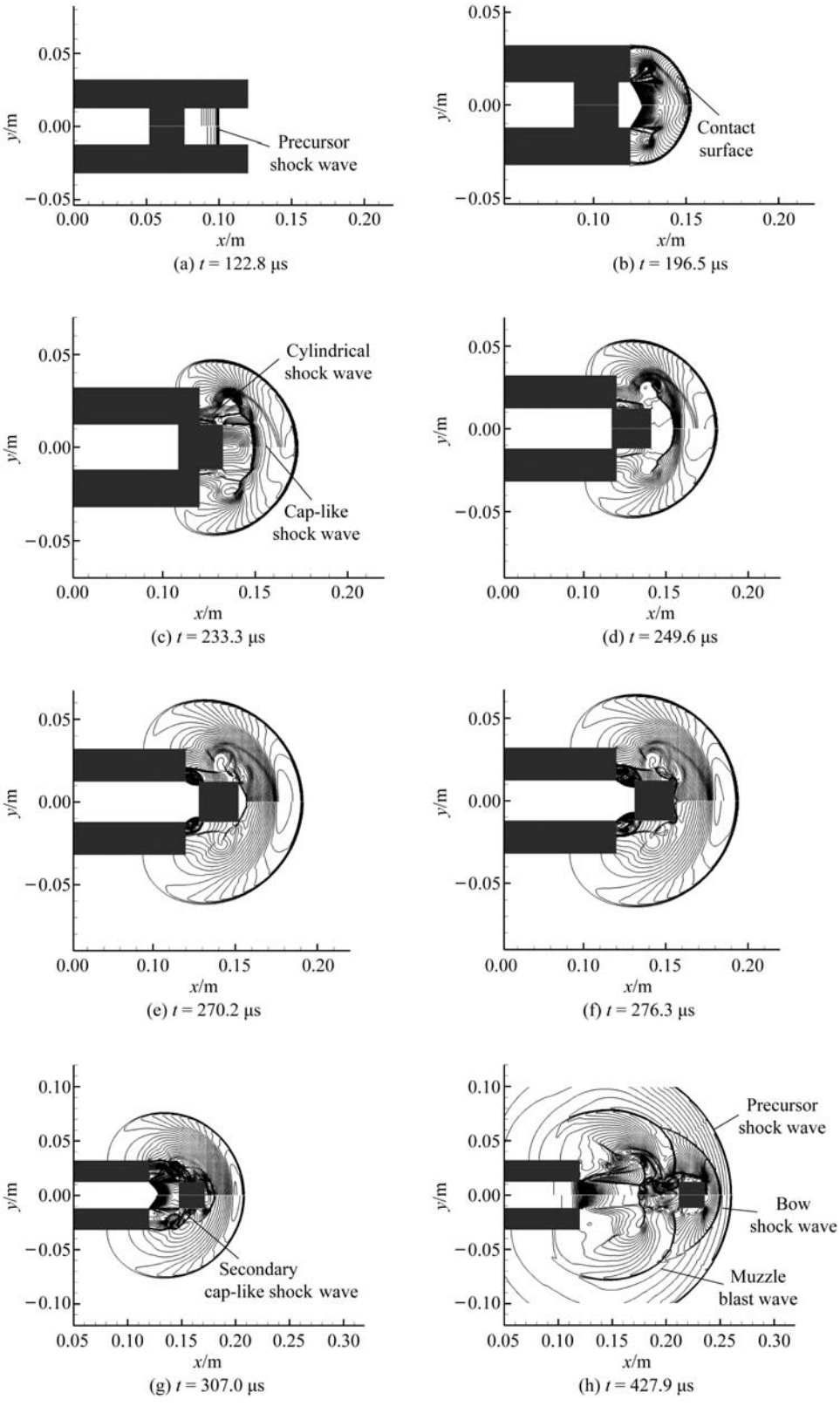

(a) t = 122.8 μs (b) t = 196.5 μs

(c) t = 233.3 μs (d) t = 249.6 μs

(e) t = 270.2 μs (f) t = 276.3 μs

(g) t = 307.0 μs (h) t = 427.9 μs

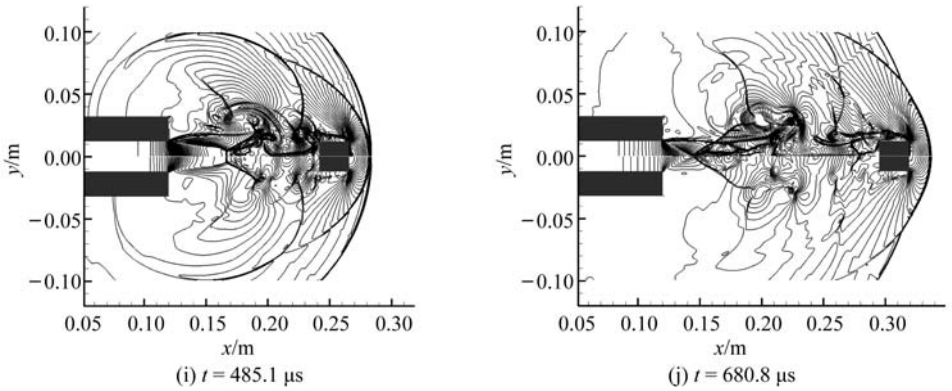

Fig. 3 Distributions of the isopycnics (the upper half) and isobars (the lower half)

a shear layer was starting from the rim of the projectile head and extending backwards due to the velocity gradient caused by the high-speed moving projectile. The muzzle blast wave caught up and intersected with the bow shock wave to form the first triple-points. The complicated and under-expanded flow pattern of the propellant gas developed and the mach stem appeared to originate from the cap-like shock wave.

In Fig. 3(i), the bow shock wave had caught up with the precursor shock wave, and the typical under-expanded jet pattern occurred in the main propellant flow field, i.e., the jet boundary (shear layer), barrel shock wave (incident shock wave), mach stem and its reflective shock wave and tangential discontinuity. The rim of the shear layer, reflective shock wave and tangential discontinuity were sucked into the primary vortex ring. In Fig. 3(j), the non-regular intersection of the barrel shock wave (incident shock wave) on the axis was transformed into a regular intersection to form an X-shaped pattern[15] due to the decrease of the intensity of the vented high-pressure gas caused by the expansion wave entering the tube. At the same time, the bow shock wave passed through the precursor shock wave to form new triple-points and cause the so-called 'sonic boom'[9]. Later, the projectile would also pass through the precursor shock and completely fly out of the range of the precursor flow field.

From Fig. 3(f) to Fig. 3(h), the intense change occurred owing to the coupling and interaction among the propellant flow field, precursor flow field and the projectile. Figure 4 is the distribution of the vorticity in the upper half and the pressure in the lower half during this process. In Fig. 4(a), the muzzle blast wave traveled over the core of the primary vortex ring (comparison to Fig. 3(g)), Although the aforementioned fold segment vanished and became smooth, the split segment close to the projectile side propagated outwards with a higher vorticity lump, framed by a dashed line circle in its vicinity in the upper half. The upper and lower part of the cap-like shock wave interacted with the projectile and the barrel shock wave, respectively, i.e., the upper part climbed over the projectile (i.e., shock wave diffraction), while the lower part intersected with the barrel shock wave. In Fig. 4(b), it is incorporated into the barrel shock wave, while the diffraction shock wave moved towards the axis. The distance between the split segment and the muzzle blast wave started to decrease for the vorticity lump framed by a dashed line circle moving upstream. In Fig. 4(c), the distance decreased rapidly, and the vorticity lump began to separte from the muzzle blast wave. The diffraction shock wave converged and reflected on the axis (i.e., the shock wave focusing), which would produce a great force to drive the projectile. In Fig. 4(d), the split section also started to become incorporated into the muzzle blast wave as the vorticity lump disengaged. From the conditions above, this process showed shockwave diffraction and focusing, and the fold, split, separation and incorporation of the muzzle blast wave front are mainly related to the vortex effect.

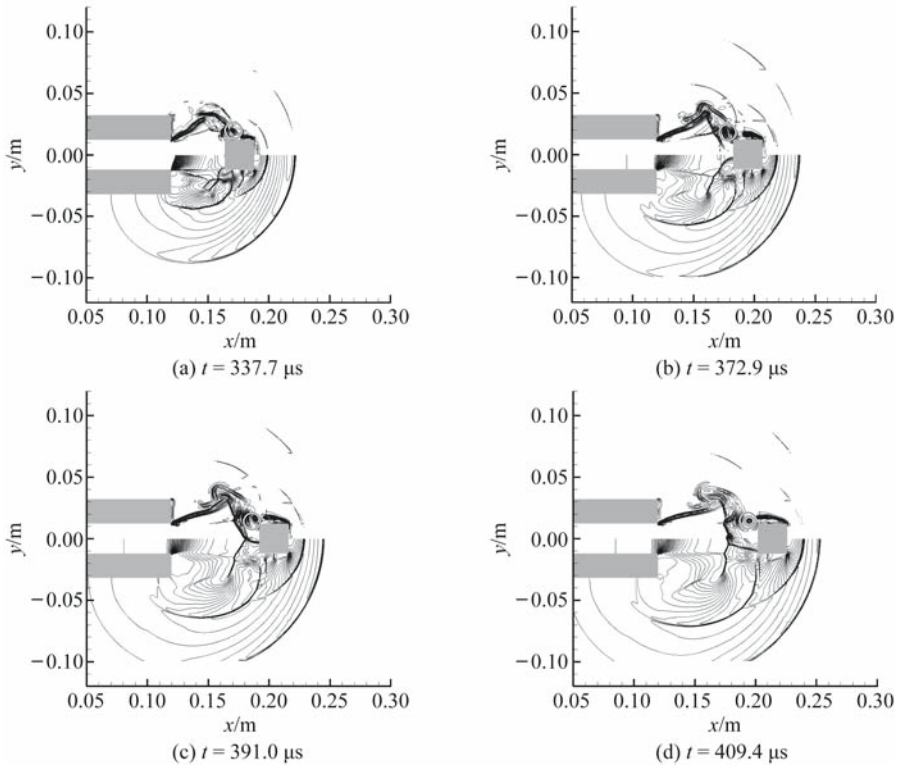

Fig. 4 Distributions of vorticity (the upper half) and pressure (the lower half)

Figure 5 shows the speed and acceleration of the projectile. Stage (A) denotes the time between the projectile head and tail reaching the exit, while (B) is the time between the tail reaching the exit and the bow shock intersecting the precursor shock. Before the projectile shoots out of the tube, the resistance force of the projectile is mainly from the friction and the precursor shock, while the driving force is from the high-pressure gas behind it. With the pressure decreasing in D_1 due to the projectile moving outwards to make its volume increase，the driving force decreased continuously and the acceleration also decreased as shown in ①–② segment of Fig. 5. When the projectile was moving outside the time stage (A), the friction force fell as the contact area descended and the projectile head entered the low pressure expansion zone (see Figs. 3(c)–(d)) of the precursor flow field. These resulted in the decrease of resistance force. If this decrease was greater than the driving force decrease, it would cause the acceleration to rise as shown in ②–③ segment of Fig. 5. If the resistance force decrease could not eliminate the decrease of the driving force, its acceleration would start to decline, as shown in point ③ of Fig. 5 (corresponding to the time in Fig. 3(c)). When the projectile was completely outside (corresponding to the time ④), its acceleration decreased rapidly due to the high-pressure gas in D_1 expanding outside, as shown in (B) time stage of Fig. 5. Its main resistance force now came, from the bow shock wave, while the driving force came from the high-pressure gas and the aforementioned shock wave diffraction and shock focusing phenomenon. The point ⑤ is the time at which the shock diffraction started to have an effect. The point ⑥ is the greatest effect of shock focusing, and then the acceleration declined again as a result of their decrease. With the projectile flying far from the tube exit, especially after the bow shock wave intersected the precursor shock wave (⑦), its fluctuation was weakened and trended toward a stable value

(⑦–⑧). Although the oscillation of projectile acceleration occurred, its speed fluctuation after the projectile rushed out is approximately negligible because of its maximal percent 7% relative to the exit speed for the whole time duration of the present case.

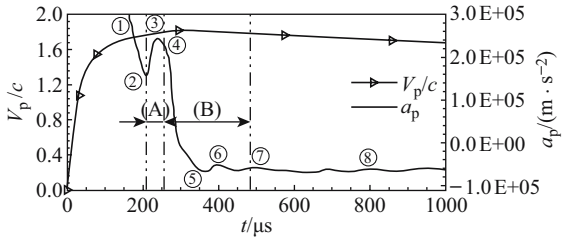

Fig. 5 Speed (V_p/c) and acceleration (a_p) of the projectile

3 Conclusion

Numerical results indicated intense coupling and interaction among the precursor flow, primary propellant flow and projectile, resulting in the production of the precursor shock, bow shock and muzzle blast wave. During this process, the interaction of the shock-shock, shock-vortex and shock diffraction, shock focusing was analyzed in detail, and factors affecting the projectile acceleration were also discussed. It is of practical importance to further understand the detailed mechanism of the muzzle flow, and it is also done obviously for the weapon industries.

References

[1] Schmidt E M, Shear D D. Optical measurements of muzzle blast[J]. *AIAA J*, 1975, **13**(8):1086–1093.

[2] Li Hongzhi,You Guozhao. Formation mechanism of the muzzle flow field with muzzle attachments and blast waves[J]. *Journal of East China Institute of Technology*, 1979, **1**(2):1–26 (in Chinese).

[3] Jiang Zonglin. Wave dynamic processed induced by a supersonic projectile discharging from a shock tube[J]. *Physics of Fluids*, 2003, **15**(6):1665–1675.

[4] Cler Daniel L, Chevaugeon Nicolas, Shephard Mark S, Flaherty Joseph E. Remacle ean-Francois. CFD application to gun muzzle blast-A validation case study[C]. AIAA 2003–1142. In: 41*st Aerospace Sciences Meeting and Exhibit*, Reno, Nevada, 2003.

[5] Settles G S, Grumstrup T P, Miller J D, Hargather M J, Dodson L J, Gatto J A. Full-scale high-speed "Edgerton" retroreflective shadowgraphy of explosions and gunshots[C]. Paper No PSFVIP-5-251. In: Milton B E (ed). *Proceedings of PSFVIP*-5, 5*th Pacific Symposium on Flow Visualisation and Image Processing*, Australia, 2005.

[6] Dayan Y, Touati D. Simulation of unsteady muzzle flow of a small-caliber gun[M]. In: Rahman M (ed). *Advances in Fluid Mechanics VI*. Skiathos, Greece, UK: WIT Press, 2006, 165–174.

[7] Cayzac R, Carette E, Alziary de Roquefort T, et al. Intermdiate ballistic computations and validations[C]. In: Niekerk C V (ed). 17*th International Symposium on Ballistics*, Midrand, South Africa: The South African Ballistics Organization, 1998, 1–8.

[8] Cayzac R, Carette E, Alziary de Roquefort T. Intermdiate ballistic unsteady sabot separation: first computations and validations[C]. In: Iris Rose Crewther (ed). 19*th International Symposium on Ballistics*, Interlaken, Switzerland, 2001, 297–305.

[9] Jiang Zonglin, Takayama K, Skews B W. Numerical study on blast flowfields induced by supersonic projectiles discharged from shock tubes[J]. *Physics of Fluids*, 1998, **10**(1):277–288.

[10] Trepanier J Y, Reggio M, Zhang H, Camarero R. A finite-volume method for the Euler equations on Arbitrary Lagrangian-Eulerian grids[J]. *Computer Fluids*, 1991, **20**(4):399–409.

[11] Leveque Randall J. Finite volume methods for hyperbolic problems[M]. Cambridge: Cambridge University Press, 2003,100–128.

[12] LeVeque R J. Wave propagation algorithms for multi-dimensional hyperbolic systems[J]. *Journal of Computational Physics*, 1997, **131**:327–353.

[13] Gillyboeuf J P, Mansuy P, Pavsic S. Two new chimera methods: application to missile separation[C]. AIAA 95–0353. In: 33*rd Aerospace Sciences Meeting and Exhibit*, Reno, NV, 1995.

[14] Menon S, Kim J H. Large-eddy simulation of afterburner flows[R]. CCL Technical Report 2002–005, Georgia Tech Computational Combustion Laboratory, Georgia Institute of Technology, Atlanta, USA. December 12, 2002. (http://www.ccl.gatech.edu/home html)

[15] Li Hongzhi, Cui Dongming, Fan Baochun. Shock wave in the continuous medium[M]. Beijing: Armament Industry Press, 1995, 58–60 (in Chinese).